
FLUIDSPLAT: Reconstructing Physical Fields from Sparse Sensors via Gaussian Primitives

Huaxi Huang¹, Meng Li^{1,2}, Zhengqing Gao^{1,3}, Xi Zhou¹, Xiaoshui Huang⁴, Xiao Sun^{1*}

¹Shanghai Artificial Intelligence Laboratory

²The Hong Kong University of Science and Technology

³Mohamed bin Zayed University of Artificial Intelligence, ⁴Shanghai Jiaotong University

Abstract

Reconstructing continuous flow fields from sparse surface-mounted sensors is central to aerodynamic design, flow control, and digital-twin instrumentation. Existing neural methods for this task typically encode sensor readings into implicit latent codes with little spatial interpretability and limited formal guidance on how representational capacity should scale with observation count. Inspired by 3D Gaussian Splatting, we introduce FLUIDSPLAT, a sensor-conditioned model that predicts K anisotropic Gaussian primitives forming a partition-of-unity scaffold, a spatially explicit and interpretable intermediate representation of the flow. For an idealized Gaussian primitive estimator, we prove an $O(K^{-s/d})$ approximation rate for fields with Sobolev smoothness s ; incorporating N noisy observations yields a squared-risk decomposition with bias $O(K^{-2s/d})$ and variance $O(\sigma^2 K/N)$. Balancing the two yields $K^* \sim (N/\sigma^2)^{d/(2s+d)}$; primitive count cannot grow freely under sparse sensing, revealing a variance bottleneck that motivates complementing the scaffold with a state-conditioned residual decoder. On a standard cylinder-flow benchmark, FLUIDSPLAT achieves the best mean error across all surface-sensor layouts; on AirfRANS with 8 surface-pressure sensors, it reduces error by 11–23% over the strongest baseline across three standard splits.

1 Introduction

Many physical systems are instrumented by a small number of sensors attached to the solid surfaces: pressure taps on an airfoil, strain gauges on a turbine blade, thermocouples on a reactor wall Manohar et al. [2018], Callaham et al. [2019], Liu et al. [2025]. Recovering the full surrounding flow field from such sparse, boundary-mounted measurements is essential for aerodynamic design, real-time control, and the construction of physical digital twins, yet it remains statistically and geometrically challenging: the observations are few, spatially confined to the boundary, and provide no direct measurements of the interior.

Several neural architectures target sparse-sensor field reconstruction directly: attention-based sensor encoders Santos et al. [2023], Voronoi-tessellation networks Fukami et al. [2021], resolution-invariant spectral models Zhao et al. [2024], Fourier-feature latent reconstruction models Nguyen et al. [2026], and shallow grid decoders Erichson et al. [2020]. In parallel, operator-learning frameworks Lu et al. [2021], Li et al. [2021], Azizzadenesheli et al. [2024] and geometry-aware or transformer-based PDE solvers Li et al. [2023a,b], Hao et al. [2023], Wu et al. [2024] have advanced surrogate modeling on irregular meshes, while differentiable sensor-placement frameworks Liu et al. [2025], Ma et al. [2025] co-optimize where to observe and how to reconstruct; however, they primarily target dense-grid, full-field, or placement-centric settings rather than reconstruction under a fixed sparse surface layout.

*Corresponding Author

For sparse surface sensing specifically, existing methods typically do not jointly provide (i) a spatially explicit state for the reconstructed field and (ii) formal characterization of how model capacity should scale with the number of observations, leaving the choice of representational complexity to heuristic tuning strategy.

These observations motivate an alternative design principle. Under sparse surface sensing, it is natural to adopt an inductive bias toward coherent spatial structures (wakes, vortices, near-wall pressure regions) that the observations can plausibly constrain, while delegating fine-scale detail to a flexible decoder. This suggests a structured primitive scaffold that organizes the recoverable spatial structure explicitly. Anisotropic Gaussian primitives are a natural basis for such a scaffold: spatially explicit, local, and parameterized by a finite set of interpretable quantities. In neural rendering, 3D Gaussian Splatting Kerbl et al. [2023] and its variants Huang et al. [2024], Yu et al. [2024] have shown that such primitives can efficiently represent radiance and geometry in visual scenes. We adopt the same representational bias for physical field reconstruction, using the primitives not as a standalone field model but as a **sensor-conditioned structured scaffold** paired with a residual decoder for the remaining correction.

Concretely, we introduce FLUIDSPLAT, a sensor-conditioned framework that represents the spatial state through K learnable anisotropic Gaussian primitives. A sensor encoder maps the sparse observations to a global context vector; a linear head projects this context into the primitive parameters (centers, anisotropic scales, weights, and amplitudes), forming a partition-of-unity field Babuška and Melenk [1997]. A Fourier-feature residual decoder Tancik et al. [2020], conditioned on the global context and scaffold state, then supplies the correction that lies beyond the primitive span. Unlike a standard latent decoder, the primitive layer yields a spatially explicit intermediate field that is sensor-conditioned; the residual decoder then refines the reconstruction beyond this scaffold.

To ground this design theoretically, we analyze idealized Gaussian primitive estimators and develop, to our knowledge, the first approximation–estimation account of splatting-style sensor-conditioned field reconstruction. The analysis separates three effects. First, unnormalized Gaussian primitive sums achieve an L^2 approximation rate $O(K^{-s/d})$ for Sobolev-regular fields. Second, the Shepard-normalized scaffold is stable and spatially explicit, but its oracle approximation saturates at first order because it reproduces constants but not higher-order polynomials. Third, when K primitive coefficients are estimated from N noisy observations, an idealized fixed-dictionary least-squares model gives a bias–variance trade-off with squared bias $O(K^{-2s/d})$ and variance $O(\sigma_{\text{noise}}^2 K/N)$. Balancing these terms yields the capacity scale $K^* \sim (N/\sigma_{\text{noise}}^2)^{d/(2s+d)}$ up to problem-dependent constants. In the sparse-sensor regime, this scale suggests that primitive capacity cannot be increased freely, motivating a compact Gaussian scaffold complemented by a residual decoder.

Empirically, FLUIDSPLAT is evaluated on two public benchmarks. On a standard cylinder-flow benchmark Santos et al. [2023] it achieves the best mean error across all surface-sensor layouts; on the published interior-8 protocol it reaches 0.0097 relative L^2 (reference value: 0.039). On AirfRANS Bonnet et al. [2022] with 8 surface-pressure sensors, it reduces error by 11–23% over the strongest baseline across three generalization splits. Ablation studies support the scaffold-plus-residual synergy: primitive-only reconstruction remains far worse than the full model, consistent with the predicted variance bottleneck. In summary, our contributions are threefold:

1. We propose FLUIDSPLAT (Section 3), a sensor-conditioned architecture that combines an explicit Gaussian primitive scaffold with a state-conditioned residual decoder for sparse-sensor flow reconstruction.
2. We develop an approximation–estimation analysis that explains the expressivity and sparse-sensing capacity limits of Gaussian primitive scaffolds, providing theoretical justification for the proposed architecture (Section 4; proofs in Appendices B–C).
3. On two public benchmarks under the reported evaluation protocols, FLUIDSPLAT achieves the best mean performance among all evaluated methods, with 11–23% error reduction on AirfRANS (Section 5).

2 Related Work

Sparse-sensor flow reconstruction. Classical approaches combine data-driven sensor placement Manohar et al. [2018] with POD-based or sparse reconstruction Callaham et al. [2019]. Neural

methods include shallow decoders from limited sensors Erichson et al. [2020], Fukami et al. [2020], Voronoi-tessellation CNNs Fukami et al. [2021], attention-based architectures that treat sensors as a sparse token set Santos et al. [2023], and Fourier-feature or spectral models for resolution-invariant reconstruction Zhao et al. [2024], Nguyen et al. [2026]. More broadly, operator-learning frameworks Lu et al. [2021], Li et al. [2021], Azzadenesheli et al. [2024] and geometry-aware PDE solvers Li et al. [2023a,b], Hao et al. [2023], Wu et al. [2024] advance surrogate modeling on general domains but are primarily developed for forward prediction with full-field supervision, although adaptable to reconstruction tasks; differentiable placement-optimization frameworks Liu et al. [2025], Ma et al. [2025] co-learn sensor locations and reconstruction and are complementary to our fixed surface-mounted sensor setting: they optimize *where* to observe, whereas we study representational capacity under a given layout. Among existing sparse-sensor methods, most encode observations into an implicit latent and decode on a grid or at query points; they typically do not jointly provide (i) a spatially explicit intermediate state and (ii) formal characterization of how representational capacity should scale with the observation count.

Gaussian primitives and neural fields. 3DGS Kerbl et al. [2023], descended from EWA splatting Zwicker et al. [2002], represents scenes via anisotropic Gaussian primitives and has become a standard in neural rendering Mildenhall et al. [2021], Huang et al. [2024], Yu et al. [2024], Chen and Wang [2026]. These primitives are spatially explicit, differentiable, and support efficient rendering and evaluation, but have been developed primarily for visual radiance and geometry. Scattered-data approximation with radial basis functions Wendland [2004], Schaback and Wendland [2006], Narcowich et al. [2005] and partition-of-unity methods Babuška and Melenk [1997] provide the classical foundation for Gaussian-kernel approximants. We are not aware of prior work that employs splatting-style primitives as a sensor-conditioned spatial scaffold for physical-field reconstruction or analyzes their capacity in this sparse-observation regime.

Approximation-theoretic context. Neural-network approximation theory Mhaskar [1996], Yarotsky [2017] and minimax estimation rates Stone [1982], Ibragimov and Has’ Minskii [2013] supply the statistical tools for analyzing Gaussian-primitive capacity. Existing sparse-sensor methods do not, to our knowledge, connect the capacity of an explicit spatial representation to observation count via a bias-variance decomposition with a K/N variance term; we provide this connection and show that it yields a variance bottleneck motivating the residual decoder.

3 FLUIDSPLAT: Method

3.1 Problem Setting

Let $\Omega \subset \mathbb{R}^d$ be a bounded Lipschitz domain and $\mathbf{f} : \Omega \rightarrow \mathbb{R}^C$ the target vector field (e.g., velocity components plus pressure, $C = d + 1$). We are given N noisy pointwise observations

$$y_i = \mathbf{f}(\mathbf{x}_i^{\text{obs}}) + \varepsilon_i, \quad i = 1, \dots, N, \quad (1)$$

with $\mathbf{x}_i^{\text{obs}}$ typically located on the body surface (e.g., surface-mounted pressure sensors) and noise satisfies mean zero $\mathbb{E}[\varepsilon_i] = 0$ and bounded variance $\text{Cov}(\varepsilon) \preceq \sigma_{\text{noise}}^2 I_N$. The task is to return a continuous reconstruction $\hat{\mathbf{f}}(\mathbf{x})$ queryable at arbitrary $\mathbf{x} \in \Omega$.

3.2 Overview

FLUIDSPLAT maps a sparse sensor set to a continuous field through three stages: (i) a *permutation-invariant sensor encoder* produces a global context vector \mathbf{z} from the unordered observation set; (ii) a linear head predicts K anisotropic Gaussian primitive parameters from \mathbf{z} , forming a normalized partition-of-unity *scaffold* field \mathbf{f}_{prim} ; (iii) a *state-conditioned residual decoder*, whose inputs include the scaffold evaluation and query-to-primitive cross-attention, supplies the correction that lies beyond the scaffold span. The scaffold is the component analyzed theoretically in Section 4; the residual decoder is motivated by the variance bottleneck identified therein.

3.3 Sensor-Conditioned Gaussian Scaffold

Primitive definition. Each of K primitives is parameterized by center $\boldsymbol{\mu}_k \in \Omega$, positive-definite precision structure Σ_k^{-1} , weight $w_k \in (0, 1)$, and amplitude $\mathbf{a}_k \in \mathbb{R}^C$. The unnormalized Gaussian

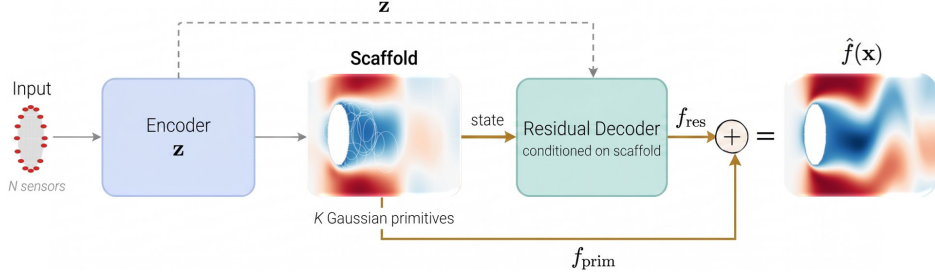


Figure 1: Overview of FLUIDSPLAT. A permutation-invariant encoder maps N surface sensors to a global context \mathbf{z} , which parameterizes K anisotropic Gaussian primitives forming the scaffold field \mathbf{f}_{prim} . A residual decoder, conditioned on the scaffold state, produces \mathbf{f}_{res} ; the final output is $\hat{\mathbf{f}}(\mathbf{x}) = \mathbf{f}_{\text{prim}}(\mathbf{x}) + \mathbf{f}_{\text{res}}(\mathbf{x})$. Insets show real model outputs on cylinder flow.

basis is

$$\varphi_k(\mathbf{x}) = \exp\left(-\frac{1}{2}(\mathbf{x} - \boldsymbol{\mu}_k)^\top \Sigma_k^{-1}(\mathbf{x} - \boldsymbol{\mu}_k)\right). \quad (2)$$

In our 2D experiments, Σ_k is parameterized by axis scales $\boldsymbol{\sigma}_k \in (0, \infty)^2$ and an optional rotation angle θ_k , giving $\Sigma_k^{-1} = R_{\theta_k}^\top \text{diag}(\boldsymbol{\sigma}_k^{-2}) R_{\theta_k}$.

Partition-of-unity field. The scaffold is a normalized mixture

$$\hat{\mathbf{f}}(\mathbf{x}) = \underbrace{\sum_{k=1}^K \psi_k(\mathbf{x}) \mathbf{a}_k}_{\mathbf{f}_{\text{prim}}(\mathbf{x})} + \underbrace{\mathbf{f}_{\text{res}}(\mathbf{x}; \mathbf{z}, \mathcal{S})}_{\text{residual decoder}}, \quad \psi_k(\mathbf{x}) = \frac{w_k \varphi_k(\mathbf{x})}{\sum_j w_j \varphi_j(\mathbf{x})}, \quad (3)$$

with $\psi_k \geq 0$, $\sum_k \psi_k = 1$, and $\mathcal{S} = \{(\boldsymbol{\mu}_k, \Sigma_k, w_k, \mathbf{a}_k)\}_{k=1}^K$ denoting the full Gaussian state. The scaffold provides a structured, spatially explicit, sensor-conditioned intermediate field: primitives provide localized degrees of freedom that can allocate support to coherent spatial structures, with parameters directly predicted from the observations. The scaffold is not intended to fully reconstruct the field by itself; rather, it exposes a structured spatial state that conditions the residual decoder.

Sensor encoder and primitive head. The encoder processes the unordered sensor set $\{(\mathbf{x}_i^{\text{obs}}, y_i)\}_{i=1}^N$ via a shared per-token MLP followed by mean and max pooling, yielding a global context $\mathbf{z} \in \mathbb{R}^D$. The aggregation is permutation-invariant and does not require changing network dimensions when the sensor count varies. A linear projection maps \mathbf{z} to all K primitive parameter vectors; for the 2D parameterization used in our experiments:

$$\{(\boldsymbol{\mu}_k, \boldsymbol{\sigma}_k, \theta_k, w_k, \mathbf{a}_k)\}_{k=1}^K = \text{Head}(\mathbf{z}), \quad (4)$$

with centers mapped via sigmoid to the normalized computational domain, scales via bounded sigmoid to $[\sigma_{\min}, \sigma_{\max}]$, and weights via sigmoid. For complex geometries, optional geometry tokens and case-metadata conditioning are fused into \mathbf{z} before the primitive head.

3.4 State-Conditioned Residual Decoder

The residual decoder refines the scaffold by receiving both global and local state information at each query point \mathbf{x} . Its input concatenates Fourier-encoded coordinates $\gamma(\mathbf{x})$ Tancik et al. [2020], the global context \mathbf{z} , and the scaffold evaluation $\mathbf{f}_{\text{prim}}(\mathbf{x})$ together with the basis mass $m(\mathbf{x}) = \sum_k w_k \varphi_k(\mathbf{x})$, which signals local scaffold support. To allow the decoder to attend directly to the primitive state, query tokens (formed from $\gamma(\mathbf{x})$ and \mathbf{z}) attend to primitive-parameter tokens via multi-head cross-attention with a residual connection and feed-forward layer. An optional learned global token projected from \mathbf{z} is appended when used.

The concatenated features are passed through an MLP to produce the residual $\mathbf{f}_{\text{res}}(\mathbf{x}; \mathbf{z}, \mathcal{S}) \in \mathbb{R}^C$. Because the decoder observes the scaffold field directly, it can condition its correction on the primitive state—coupling the two components so that the scaffold provides structured degrees of freedom while

the decoder supplies the remaining detail beyond the scaffold span. The core architecture is shared across all experiments; dataset-specific information enters only through lightweight conditioning channels: the covariance parameterization of the Gaussian state, and optional per-query geometry or metadata features when such quantities are part of the benchmark protocol (Appendix F).

3.5 Training and Inference

Training. We train end-to-end with full-field supervision at randomly sampled query points plus a soft sensor-consistency term:

$$\mathcal{L} = \mathbb{E}_{\mathbf{x} \sim \Omega} \left\| \hat{\mathbf{f}}(\mathbf{x}) - \mathbf{f}(\mathbf{x}) \right\|^2 + \lambda_{\text{obs}} \frac{1}{N} \sum_i \left\| \hat{\mathbf{f}}(\mathbf{x}_i^{\text{obs}}) - y_i \right\|^2. \quad (5)$$

Inference. At test time only the N sensor readings are provided; the model produces a continuous field queryable at any resolution or mesh. All hyperparameters and dataset-specific conditioning details are given in Appendix F and H.

4 Theoretical Analysis

This section states the main results. Full proofs, the dimension-specific analysis, and the connection to Navier–Stokes regularity are in Appendices B–E.

Let $\Omega \subset \mathbb{R}^d$ be the bounded spatial domain, d the spatial dimension, and s the Sobolev regularity of the target field. We write $a \lesssim b$ when $a \leq Cb$, where C is independent of the primitive count K , sensor count N , and noise level σ_{noise} . Geometric assumptions on primitive centers μ_k , including fill distance h , separation distance q , and quasi-uniformity, are stated only when needed and formalized in Appendix A.

4.1 Representational Capacity

Theorem 1 (Gaussian primitive approximation). *Let $\Omega \subset \mathbb{R}^d$ be a bounded Lipschitz domain and let $\varepsilon > 0$. For every $f \in H^{s+\varepsilon}(\Omega)$ with $s > 0$ and every $K \geq 1$, there exists a K -term unnormalized Gaussian approximant $g_K = \sum_k c_k \varphi_k$ such that*

$$\|f - g_K\|_{L^2(\Omega)} \leq C_{\varepsilon, s, d, \Omega} K^{-s/d} \|f\|_{H^{s+\varepsilon}(\Omega)}. \quad (6)$$

The vector-valued case $\mathbf{f} \in H^{s+\varepsilon}(\Omega; \mathbb{R}^C)$ follows componentwise.

The arbitrarily small $\varepsilon > 0$ is the technical cost of passing from Sobolev spaces to the nonlinear Gaussian approximation class. The proof specializes nonlinear Gaussian-network approximation rates of Hangelbroek and Ron Hangelbroek and Ron [2010] to bounded Lipschitz domains via a Sobolev embedding argument; see Appendix B.

Proposition 2 (Partition-of-unity saturation). *Assume that the Gaussian centers are quasi-uniform, the weight satisfy $0 < w_- \leq w_k \leq w_+ < \infty$, and the Gaussian covariances are comparable to the squared fill distance $\Sigma_k \asymp h_K^2 I$. For $f \in H^s(\Omega)$, $s > 1 + d/2$, the oracle scaffold f_{prim} in (3), with $a_k = f(\mu_k)$, satisfies*

$$\|f - f_{\text{prim}}\|_{L^2(\Omega)} \lesssim K^{-1/d} \|f\|_{H^s(\Omega)}.$$

The first-order saturation reflects zeroth-order polynomial reproduction of the partition of unity, necessitating a residual component for higher-order correction.

Remark 3 (Scope of novelty). Theorem 1 specializes existing nonlinear Gaussian approximation theory to the primitive scaffold used in FLUIDSPLAT, while Proposition 2 isolates the first-order saturation of the Shepard-normalized field. Together with the estimation analysis below, these results provide, to our knowledge, the first approximation–estimation account of splatting-style sensor-conditioned field reconstruction, linking Gaussian primitive count to observation noise through an explicit capacity scaling.

4.2 Variance Bottleneck

Ordinary least squares. Let $V_K = \text{span}\{\varphi_k\}_{k=1}^K$ be a K -dimensional Gaussian dictionary with fixed centers μ_k and precision matrices Σ_k^{-1} . Only the linear coefficients are estimated from data. Assume that the observation matrix $\mathbf{A} \in \mathbb{R}^{N \times K}$, $A_{ij} = \varphi_j(\mathbf{x}_i^{\text{obs}})$ has full column rank. Let $\mathbf{G} \in \mathbb{R}^{K \times K}$ with $G_{jl} = \int_{\Omega} \varphi_j \varphi_l d\mathbf{x}$ denote the Gram matrix and $r_X := (r_1, \dots, r_N)^\top$ with $r_i = f(x_i) - f_K^*(x_i)$ denote the approximation residual. Define the least-squares estimator

$$\hat{f}_K(x) = \sum_{k=1}^K \hat{c}_k \varphi_k(x), \text{ where } \hat{c} = \arg \min_{c \in \mathbb{R}^K} \frac{1}{N} \sum_{i=1}^N \left(y_i - \sum_{k=1}^K c_k \varphi_k(x_i) \right)^2.$$

Theorem 4 (Bias–variance bound). *Assume (i) the fixed dictionary V_K admits the approximation bound; (ii) the samples are spectrally stable $\mathbf{A}^\top \mathbf{A} \asymp N\mathbf{G}$; (iii) the approximation residual at sensor locations is controlled $\|r_X\|_2/\sqrt{N} \lesssim \|r\|_{L^2(\Omega)}$. Then*

$$\mathbb{E} \left\| \mathbf{f} - \hat{\mathbf{f}}_K \right\|_{L^2}^2 \leq \underbrace{C_{\text{bias}} K^{-2s/d} \|\mathbf{f}\|_{H^{s+\varepsilon}}^2}_{\text{bias}^2} + \underbrace{C_{\text{var}} \sigma_{\text{noise}}^2 K/N}_{\text{variance}}. \quad (7)$$

where C_{bias} and C_{var} are constants independent of $K, N, \sigma_{\text{noise}}$.

Corollary 5 (Capacity scale). *Minimizing the upper bound in (7) gives*

$$K^* \sim (N/\sigma_{\text{noise}}^2)^{d/(2s+d)} \|\mathbf{f}\|_{H^{s+\varepsilon}}^{2d/(2s+d)}, \quad (8)$$

At this scale,

$$\mathbb{E} \|\mathbf{f} - \hat{\mathbf{f}}_{K^*}\|_{L^2(\Omega)}^2 \lesssim \left(\frac{\sigma_{\text{noise}}^2}{N} \right)^{2s/(2s+d)} \|\mathbf{f}\|_{H^{s+\varepsilon}}^{2d/(2s+d)}.$$

Remark 6 (Why residual decoders help). Increasing K reduces approximation bias by enlarging the Gaussian dictionary, but it also increases the number of coefficients estimated from noisy observations. In the fixed-dictionary least-squares model, this produces a variance term proportional to K/N . The resulting capacity scale suggests that, under sparse sensing, the primitive field should remain compact. This motivates using the Gaussian primitives as a spatial scaffold, with the residual decoder modeling corrections not captured by this low-dimensional component.

5 Experiments

Datasets. *Senseiver cylinder:* 2D cylinder vorticity benchmark, evaluated under (a) the official interior-8 protocol Santos et al. [2023] and (b) our surface-4/8/16 layouts on the cylinder wall. *AirFRANS* Bonnet et al. [2022]: 2D RANS airfoil simulations with surface-pressure sensors uniformly spaced in arclength; three splits — Full, AoA-shift, Re-shift. AirFRANS and cylinder-surface results use fixed layouts and five training seeds; the interior-8 Senseiver baseline is quoted from the published paper. Relative L^2 error is the primary metric. See Appendix F for complete details.

Baselines. *Senseiver official* for the cylinder protocol (official code adapted to the surface layouts with a training-length sweep, detailed in Appendix G); *Senseiver official-adapter* for AirFRANS; *DeepONet*; and two operator-style re-implementations (*RecFNO* and *FLRONet*, labeled “reimpl.” throughout). POD-Ridge is included for AirFRANS as a classical baseline.

Reporting convention. Unless explicitly stated otherwise, main-table entries report the mean and standard deviation over training seeds. When a best-of-five value is shown in parentheses, it is provided only to compare with single-run reporting conventions; rankings are based on seed means.

Evaluation order. We present results from simple to realistic. The Senseiver cylinder benchmark is a controlled 2D proof-of-concept where the flow geometry, field variable, and train/test split are simple enough to isolate the sensing architecture. AirFRANS is the more realistic aerodynamic benchmark: irregular meshes, airfoil geometry, multiple physical channels, and out-of-distribution AoA/Reynolds splits make it the stronger test of robustness.

Table 1: Controlled cylinder benchmark. Relative L^2 is evaluated on 4,950 test frames. Interior-8 uses the official Senseiver sensor layout and protocol; the Senseiver entry is the published value, while all other Interior-8 entries are single-run local evaluations under the same protocol. Surface columns report mean \pm seed std over seeds $\{123, \dots, 127\}$. Ranking is by seed mean for surface results; lower is better.

Method	Interior-8 (protocol)	Surface-4	Surface-8	Surface-16
FLUIDSPLAT (ours)	0.0097	0.0642 \pm 0.0041	0.0358 \pm 0.0073	0.0160 \pm 0.0008
Senseiver official	0.039	0.0759 \pm 0.0121	0.0580 \pm 0.0071	0.0556 \pm 0.0109
DeepONet	0.3847	0.0925 \pm 0.0034	0.1301 \pm 0.0137	0.0946 \pm 0.0023
FLRONet (reimpl.)	0.3715	0.0693 \pm 0.0066	0.0678 \pm 0.0099	0.0460 \pm 0.0037
RecFNO (reimpl.)	0.0875	0.0745 \pm 0.0162	0.1024 \pm 0.0112	0.0705 \pm 0.0056

Table 2: AirfRANS main results, 8-sensor surface-pressure layout, five training seeds. Lower is better; best in bold.

Method	Full-8	AoA-8	Reynolds-8
FLUIDSPLAT (ours)	0.2518 \pm 0.0389	0.5280 \pm 0.1010	0.3129 \pm 0.0229
DeepONet	0.3289 \pm 0.0330	0.5937 \pm 0.0991	0.3859 \pm 0.0183
Senseiver official-adapter	0.3891 \pm 0.0311	0.7546 \pm 0.0904	0.4647 \pm 0.0674
RecFNO (reimpl.)	0.3939 \pm 0.0503	0.8078 \pm 0.1297	0.4400 \pm 0.0404
FLRONet (reimpl.)	0.4339 \pm 0.0323	0.8013 \pm 0.0706	0.4710 \pm 0.0461
POD-Ridge	0.5849	1.2982	0.6024

5.1 Senseiver Cylinder: Controlled Concept Validation

Table 1 compares methods on the Senseiver cylinder benchmark under the official interior-8 protocol and our new surface-sensor protocol. For Interior-8, we report FLUIDSPLAT under the same layout and evaluation metric and quote the published Senseiver value 0.039 Santos et al. [2023] as the official reference. Under the surface protocol, FLUIDSPLAT obtains the best five-seed mean for every sensor count. Exact per-seed surface results are provided in Appendix H; the main table reports seed-level statistics.

5.2 AirfRANS: Realistic Sparse Surface-Pressure Reconstruction

Table 2 reports the primary metric (clean reconstruction, mean \pm std over 5 seeds) on the 8-sensor surface-pressure layout. FLUIDSPLAT is the best method in every setting with 11.1–23.4% relative improvement over the strongest non-ours baseline. Relative to the Senseiver official-adapter baseline, the improvement is 30.0–35.3% across the three splits.

Sensor-count scaling. Table 3 shows the sensor-count curve. FLUIDSPLAT improves sharply from 4 to 8 sensors and remains consistently better than DeepONet at 12 and 16. The curve is interpreted conservatively: the 8-sensor layout was tuned more heavily than the 12/16 layouts, so the non-monotone trend suggests that placement and model capacity matter in addition to sensor count.

5.3 Theory Validation, Ablations, and Cost

Theory validation. We separate theory-facing diagnostics from the benchmark tables. The oracle experiment in Figure 2 (left) fixes quasi-uniform centers on the Senseiver cylinder data, reads amplitudes directly from the full field, and removes optimization noise. The raw vorticity field converges slowly due to high-frequency structure; controlled smoothing moves the empirical exponent toward the $K^{-1/2}$ first-order reference predicted by Proposition 2 (details in Appendix H).

K-sweep. Figure 2 (right) shows the trained model on Surface-8 as K varies. Primitive-only error improves with K (bias reduction), while the full model is best at $K = 64$ (0.0282) and degrades at larger K (0.0358 at $K = 384$). This pattern is consistent with the bias–variance trade-off of Corollary 5: the idealized bound predicts a small optimal primitive count when $N = 8$. This supports the view of Gaussian primitives as a structured scaffold rather than a standalone solution. The sweep

Table 3: AirfRANS sensor-count curve (5 seeds). The 8-sensor position is tuned; 4/12/16 use analogous arclength schedules.

# Sensors	4	8	12	16
FLUIDSPLAT (ours)	0.2997 ± 0.0328	0.2518 ± 0.0389	0.2833 ± 0.0369	0.2813 ± 0.0521
DeepONet	0.3108 ± 0.0215	0.3289 ± 0.0330	0.3320 ± 0.0121	0.3171 ± 0.0312

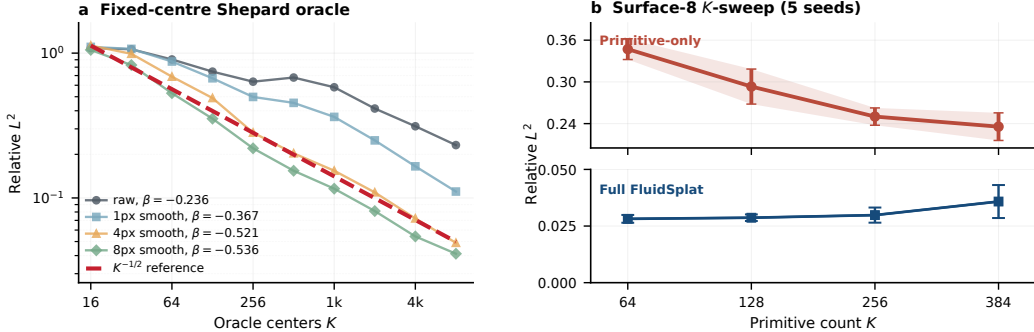


Figure 2: Theory validation on the Senseiver cylinder data. Left: fixed-center Gaussian Shepard oracle on raw and smoothed vorticity frames; controlled smoothing moves the empirical exponent toward the $K^{-1/2}$ first-order reference. Right: Surface-8 trained K -sweep (five seeds). Primitive-only error improves with K (bias reduction), while the full model is best at $K = 64$ and degrades at larger K , consistent with the bias–variance trade-off of Corollary 5. The main table uses $K = 384$; the sweep is a single-axis diagnostic. Exact numbers in Appendix H.

holds all non- K hyperparameters fixed at their jointly tuned $K = 384$ values; it is a single-axis diagnostic, not a full configuration search. The main cylinder table retains the $K = 384$ configuration.

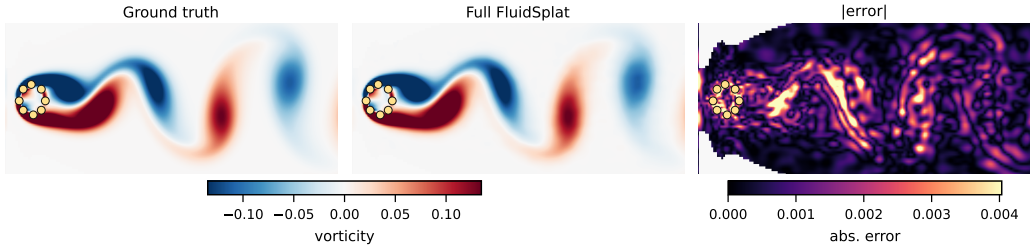


Figure 3: Senseiver cylinder Surface-8 qualitative example. Panels show ground truth, full FLUIDSPLAT, and absolute error for a held-out vorticity frame. Gold dots are the cylinder-wall sensors. The full model recovers the alternating vortex street from sparse surface readings, while the remaining errors concentrate near high-gradient wake structures.

Ablation studies. We use AirfRANS Full-8 as the primary ablation dataset because it is the hardest and most realistic setting in the paper: unstructured airfoil meshes, geometry-conditioned inputs, three physical output channels, and surface-only pressure observations. Cylinder Surface-8 is kept as an auxiliary sanity check in the appendix. The controlled AirfRANS ablations remove one design component at a time: (i) the Gaussian primitive contribution, (ii) the residual decoder, (iii) query-to-state cross-attention, (iv) global-token/state-feature conditioning, and (v) observation-consistency loss. The intended interpretation is not merely that FLUIDSPLAT has more parameters, but that explicit Gaussian state plus an attention-conditioned residual decoder improves sparse-sensor reconstruction under matched training data and evaluation metrics. In particular, the Gaussian primitive field is not presented as a standalone universal solution; it is a structured, interpretable spatial scaffold whose best performance comes from being paired with the residual decoder. The ablation uses three seeds as a controlled diagnostic.

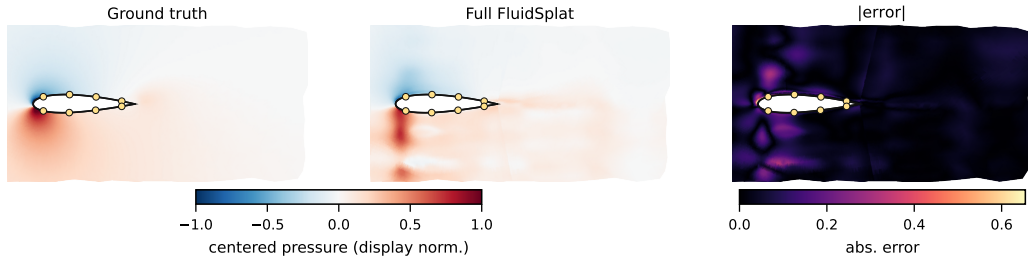


Figure 4: AirfRANS Full-8 qualitative example. Panels show ground truth, full FLUIDSPLAT, and absolute error for display-normalized centered pressure. Gold dots are the eight surface-pressure sensors.

Table 4: Controlled AirfRANS Full-8 ablation. Each row changes one component of the selected FLUIDSPLAT configuration and reports test clean reconstruction error over seeds 1–3 under the same model family and controlled ablation protocol (the main table reports the final 5-seed benchmark configuration). Lower is better.

Variant	Parameters	clean_recon_full
Full FLUIDSPLAT	0.236M	0.2367 ± 0.0451
w/o global token	0.212M	0.2759 ± 0.0358
w/o state features	0.235M	0.2992 ± 0.0171
w/o query-to-state attention	0.210M	0.3446 ± 0.0143
residual-only (no primitive output)	0.209M	0.3530 ± 0.0130
primitive-only (no residual decoder)	0.114M	0.6524 ± 0.0158
w/o observation consistency	0.236M	0.2620 ± 0.0121

Table 5: Model size and inference cost on AirfRANS Full-8. Forward time is end-to-end (sensor encoding, primitive prediction, and query decoding) with batch size 1 and 16,384 query points on the same GPU. This table is reported on AirfRANS rather than cylinder because AirfRANS exercises the full multi-channel, geometry-conditioned architecture.

Method	Parameters	Forward time (ms)
FLUIDSPLAT (ours)	0.236M	2.57 ± 0.20
DeepONet	0.325M	2.02 ± 0.28
RecFNO (reimpl.)	17.136M	3.63 ± 0.97
FLRONet (reimpl.)	1.332M	2.59 ± 0.17
Senseiver official-adapter	0.945M	6.12 ± 0.75

Qualitative reconstruction. Figures 3–4 show end-to-end reconstructions. The AirfRANS panel displays the reconstruction and error on an irregular airfoil mesh; the cylinder panel provides the corresponding view on the regular vorticity grid (the learned primitive scaffold is deferred to Appendix I). Error maps show that remaining mistakes concentrate in high-gradient regions near the body and wake, consistent with the theory diagnostic and ablations.

6 Conclusion

We introduced FLUIDSPLAT, pairing a Gaussian primitive scaffold with a state-conditioned residual decoder for sparse-sensor flow reconstruction. The accompanying theory identifies a first-order saturation of the normalized scaffold and a variance bottleneck on primitive capacity, jointly justifying the architecture design. FLUIDSPLAT achieves the best mean error on both benchmarks tested.

Limitation and Discussion. Our empirical scope is 2D; the theory is dimension-parametric (Appendix D), but validating unsteady 3D fields is left for future work. The optimal least square analysis fixes primitive centers and uses an idealized observation model, serving as a mechanistic guide rather than a finite-sample guarantee. Because sparse-sensor reconstructions may enter safety-critical loops, uncertainty calibration remains an important companion.

References

- Kamyar Azizzadenesheli, Nikola Kovachki, Zongyi Li, Miguel Liu-Schiaffini, Jean Kossaifi, and Anima Anandkumar. Neural operators for accelerating scientific simulations and design. *Nature Reviews Physics*, 6(5):320–328, 2024. doi: 10.1038/s42254-024-00712-5.
- Ivo Babuška and Jens M Melenk. The partition of unity method. *International journal for numerical methods in engineering*, 40(4):727–758, 1997.
- Florent Bonnet, Jocelyn Mazari, Paola Cinnella, and Patrick Gallinari. Airfrans: High fidelity computational fluid dynamics dataset for approximating reynolds-averaged navier–stokes solutions. volume 35, pages 23463–23478, 2022.
- Jared L Callahan, Kazuki Maeda, and Steven L Brunton. Robust flow reconstruction from limited measurements via sparse representation. *Physical Review Fluids*, 4(10):103907, 2019.
- Guikun Chen and Wenguan Wang. A survey on 3d gaussian splatting. *ACM Comput. Surv.*, April 2026. ISSN 0360-0300. doi: 10.1145/3807511. URL <https://doi.org/10.1145/3807511>. Just Accepted.
- N Benjamin Erichson, Lionel Mathelin, Zhewei Yao, Steven L Brunton, Michael W Mahoney, and J Nathan Kutz. Shallow neural networks for fluid flow reconstruction with limited sensors. *Proceedings of the Royal Society A: Mathematical, Physical and Engineering Sciences*, 476(2238), 2020.
- Kai Fukami, Koji Fukagata, and Kunihiro Taira. Assessment of supervised machine learning methods for fluid flows: K. fukami et al. *Theoretical and Computational Fluid Dynamics*, 34(4):497–519, 2020.
- Kai Fukami, Romit Maulik, Nesar Ramachandra, Koji Fukagata, and Kunihiro Taira. Global field reconstruction from sparse sensors with voronoi tessellation-assisted deep learning. *Nature Machine Intelligence*, 3(11):945–951, 2021.
- Vivette Girault and Pierre-Arnaud Raviart. Finite element methods for navier-stokes equations: theory and algorithms. *NASA STI/Recon Technical Report A*, 87:52227, 1986.
- Pierre Grisvard. *Elliptic problems in nonsmooth domains*. SIAM, 2011.
- Thomas Hangelbroek and Amos Ron. Nonlinear approximation using gaussian kernels. *Journal of Functional Analysis*, 259(1):203–219, 2010.
- Zhongkai Hao, Zhengyi Wang, Hang Su, Chengyang Ying, Yinpeng Dong, Songming Liu, Ze Cheng, Jian Song, and Jun Zhu. Gnot: A general neural operator transformer for operator learning. In *International conference on machine learning*, pages 12556–12569. PMLR, 2023.
- Binbin Huang, Zehao Yu, Anpei Chen, Andreas Geiger, and Shenghua Gao. 2d gaussian splatting for geometrically accurate radiance fields. In *ACM SIGGRAPH 2024 conference papers*, pages 1–11, 2024.
- Ildar Abdulovich Ibragimov and Rafail Zalmanovich Has’ Minskii. *Statistical estimation: asymptotic theory*. Springer Science & Business Media, 2013.
- Bernhard Kerbl, Georgios Kopanas, Thomas Leimkuehler, and George Drettakis. 3d gaussian splatting for real-time radiance field rendering. *ACM Transactions on Graphics*, 42(4):1–14, 2023. doi: 10.1145/3592433.
- V Kozlov, V Maz’ya, and J Rossmann. Spectral problems associated with corner singularities of solutions to elliptic equations. *Mathematical Surveys and Monographs*, 2000.
- Zongyi Li, Nikola Borislavov Kovachki, Kamyar Azizzadenesheli, Burigede liu, Kaushik Bhattacharya, Andrew Stuart, and Anima Anandkumar. Fourier neural operator for parametric partial differential equations. In *International Conference on Learning Representations*, 2021. URL <https://openreview.net/forum?id=c8P9NQVtmm0>.

- Zongyi Li, Daniel Zhengyu Huang, Burigede Liu, and Anima Anandkumar. Fourier neural operator with learned deformations for pdes on general geometries. *Journal of Machine Learning Research*, 24(388):1–26, 2023a.
- Zongyi Li, Nikola Kovachki, Chris Choy, Boyi Li, Jean Kossaifi, Shourya Otta, Mohammad Amin Nabian, Maximilian Stadler, Christian Hundt, Kamyar Azizzadenesheli, et al. Geometry-informed neural operator for large-scale 3d pdes. volume 36, pages 35836–35854, 2023b.
- Xu Liu, Wei Peng, Xiaoya Zhang, Xiaoyu Zhao, Weien Zhou, Wen Yao, and Xiaoqian Chen. Enhancing deep learning-based field reconstruction with a differentiable learning framework. *Nature Machine Intelligence*, 7(7):1129–1140, 2025.
- Lu Lu, Pengzhan Jin, Guofei Pang, Zhongqiang Zhang, and George Em Karniadakis. Learning nonlinear operators via deepnet based on the universal approximation theorem of operators. *Nature machine intelligence*, 3(3):218–229, 2021.
- Yuezhou Ma, Haixu Wu, Hang Zhou, Huikun Weng, Jianmin Wang, and Mingsheng Long. Physense: Sensor placement optimization for accurate physics sensing. *arXiv preprint arXiv:2505.18190*, 2025.
- Krithika Manohar, Bingni W Brunton, J Nathan Kutz, and Steven L Brunton. Data-driven sparse sensor placement for reconstruction: Demonstrating the benefits of exploiting known patterns. *IEEE Control Systems Magazine*, 38(3):63–86, 2018.
- Hrushikesh N Mhaskar. Neural networks for optimal approximation of smooth and analytic functions. *Neural computation*, 8(1):164–177, 1996.
- Ben Mildenhall, Pratul P Srinivasan, Matthew Tancik, Jonathan T Barron, Ravi Ramamoorthi, and Ren Ng. Nerf: Representing scenes as neural radiance fields for view synthesis. *Communications of the ACM*, 65(1):99–106, 2021.
- Francis Narcowich, Joseph Ward, and Holger Wendland. Sobolev bounds on functions with scattered zeros, with applications to radial basis function surface fitting. *Mathematics of Computation*, 74(250):743–763, 2005.
- Phong CH Nguyen, Joseph B Choi, and Quang-Trung Luu. Deep learning with fourier features for regressive flow field reconstruction from sparse sensor measurements. *Scientific Reports*, 2026.
- Jooyoung Park and Irwin W Sandberg. Universal approximation using radial-basis-function networks. *Neural computation*, 3(2):246–257, 1991.
- Javier E Santos, Zachary R Fox, Arvind Mohan, Daniel O’Malley, Hari Viswanathan, and Nicholas Lubbers. Development of the senseiver for efficient field reconstruction from sparse observations. *Nature Machine Intelligence*, 5(11):1317–1325, 2023.
- Robert Schaback and Holger Wendland. Kernel techniques: from machine learning to meshless methods. *Acta numerica*, 15:543–639, 2006.
- Donald Shepard. A two-dimensional interpolation function for irregularly-spaced data. In *Proceedings of the 1968 23rd ACM national conference*, pages 517–524, 1968.
- Charles J Stone. Optimal global rates of convergence for nonparametric regression. *The annals of statistics*, pages 1040–1053, 1982.
- Matthew Tancik, Pratul Srinivasan, Ben Mildenhall, Sara Fridovich-Keil, Nithin Raghavan, Utkarsh Singhal, Ravi Ramamoorthi, Jonathan Barron, and Ren Ng. Fourier features let networks learn high frequency functions in low dimensional domains. volume 33, pages 7537–7547, 2020.
- Roger Temam. *Navier–Stokes equations: theory and numerical analysis*, volume 343. American Mathematical Society, 2024.
- Holger Wendland. *Scattered data approximation*, volume 17. Cambridge university press, 2004.

- Haixu Wu, Huakun Luo, Haowen Wang, Jianmin Wang, and Mingsheng Long. Transolver: A fast transformer solver for pdes on general geometries. In *International Conference on Machine Learning*, pages 53681–53705. PMLR, 2024.
- Dmitry Yarotsky. Error bounds for approximations with deep relu networks. *Neural networks*, 94: 103–114, 2017.
- Zehao Yu, Anpei Chen, Binbin Huang, Torsten Sattler, and Andreas Geiger. Mip-splatting: Alias-free 3d gaussian splatting. In *Proceedings of the IEEE/CVF conference on computer vision and pattern recognition*, pages 19447–19456, 2024.
- Xiaoyu Zhao, Xiaoqian Chen, Zhiqiang Gong, Weien Zhou, Wen Yao, and Yunyang Zhang. Recfno: A resolution-invariant flow and heat field reconstruction method from sparse observations via fourier neural operator. *International Journal of Thermal Sciences*, 195:108619, 2024.
- Matthias Zwicker, Hanspeter Pfister, Jeroen van Baar, and Markus Gross. EWA splatting. *IEEE Transactions on Visualization and Computer Graphics*, 8(3):223–238, 2002. doi: 10.1109/TVCG.2002.1021576.

A Notation and Preliminaries

Asymptotic notation For symmetric positive semidefinite matrices A and B , we write $A \asymp B$ if there exist constants $c_1, c_2 > 0$ independent of the main parameters, such that

$$c_1 B \preceq A \preceq c_2 B.$$

where the inequalities are understood in the positive semidefinite sense. For nonnegative scalars, we write $a \lesssim b$ if $a \leq Cb$ for a constant C independent of the main parameters, and $a \asymp b$ if both $a \lesssim b$ and $b \lesssim a$ hold.

Gaussian primitive classes. Let φ_k denote a Gaussian basis function of the form in (2). Denote $\mathbf{g}_K(\mathbf{x}) = \sum_{k=1}^K c_k \varphi_k(\mathbf{x})$ as a K -term unnormalized Gaussian primitive as in (2). Then denote this class as $\mathcal{G}_K = \{g_K; c_k, \mu_k, \sigma_k\}$. Also, we denote the normalized Gaussian primitive class as $\mathcal{F}_K = \{f_K = \sum_{k=1}^K \psi_k(\mathbf{x}) \mathbf{a}_k\}$ as in 3.

Quasi-uniformity. Let $X_K = \{\mu_k\}_{k=1}^K \subset \Omega$ be a set of centers in a bounded Lipschitz domain $\Omega \subset \mathbb{R}^d$. Its fill distance and separation radius are

$$h_K := \sup_{\mathbf{x} \in \Omega} \min_{1 \leq k \leq K} \|\mathbf{x} - \mu_k\|, \quad q_K := \frac{1}{2} \min_{i \neq j} \|\mu_i - \mu_j\|.$$

A family $\{X_K\}_{K \geq 1}$ is quasi-uniform if there exists a constant $\rho < \infty$, independent of K , such that $h_K \leq \rho q_K$. On a fixed bounded Lipschitz domain, quasi-uniformity implies $h_K \asymp K^{-1/d}$, with constants depending only on Ω , d , and ρ Wendland [2004].

B Approximation Theory

B.1 Universal Approximation

Proposition 7 (Universal approximation). *The unions $\bigcup_{K \geq 1} \mathcal{G}_K$ and $\bigcup_{K \geq 1} \mathcal{F}_K$ are dense in $L^2(\Omega; \mathbb{R}^C)$.*

Proof. For the unnormalized class, density follows from the universal approximation theorem for Gaussian RBF networks Park and Sandberg [1991]: finite linear combinations of Gaussian radial basis functions are uniformly dense in $C(\bar{\Omega})$. Applying the scalar result componentwise gives density in $C(\bar{\Omega}; \mathbb{R}^C)$. Since $C(\bar{\Omega}; \mathbb{R}^C)$ is dense in $L^2(\Omega; \mathbb{R}^C)$, the union $\bigcup_{K \geq 1} \mathcal{G}_K$ is dense in $L^2(\Omega; \mathbb{R}^C)$.

For the normalized class, first take $\mathbf{f} \in C(\bar{\Omega}; \mathbb{R}^C)$. Choose quasi-uniform centers $X_K = \{\mu_k\}_{k=1}^K$ with fill distance $h_K \rightarrow 0$, set Gaussian scales $\sigma_K \asymp h_K$, take $w_k = 1$, and set $\mathbf{a}_k = \mathbf{f}(\mu_k)$. The weights are nonnegative and satisfy $\sum_{k=1}^K \psi_k(\mathbf{x}) = 1$. Hence

$$\mathbf{f}_K(\mathbf{x}) - \mathbf{f}(\mathbf{x}) = \sum_{k=1}^K \psi_k(\mathbf{x}) (\mathbf{f}(\mu_k) - \mathbf{f}(\mathbf{x})).$$

By the classical Shepard approximation argument Shepard [1968], $\mathbf{f}_K \rightarrow \mathbf{f}$ uniformly on $\bar{\Omega}$: the contribution from nearby centers is controlled by the modulus of continuity of \mathbf{f} , while the contribution from distant centers vanishes uniformly by Gaussian decay and quasi-uniform packing. Therefore $\bigcup_{K \geq 1} \mathcal{F}_K$ is dense in $C(\bar{\Omega}; \mathbb{R}^C)$, and hence dense in $L^2(\Omega; \mathbb{R}^C)$. \square

B.2 Proof of Theorem 1

We prove (6) for scalar f using isotropic Gaussian networks; the vector case follows componentwise.

Proof. By the extension theorem for bounded Lipschitz domains, there exists a bounded extension operator E such that $Ef|_{\Omega} = f$ and

$$\|Ef\|_{H^{s+\varepsilon}(\mathbb{R}^d)} \leq C_{\Omega} \|f\|_{H^{s+\varepsilon}(\Omega)}.$$

Using the standard identification $H^{s+\varepsilon}(\mathbb{R}^d) = F_{2,2}^{s+\varepsilon}(\mathbb{R}^d)$ and the Triebel–Lizorkin embedding

$$F_{2,2}^{s+\varepsilon}(\mathbb{R}^d) \hookrightarrow F_{\tau,q}^s(\mathbb{R}^d), \quad \frac{1}{\tau} = \frac{1}{2} + \frac{s}{d}, \quad \frac{1}{q} = 1 + \frac{s}{d}$$

we obtain

$$|Ef|_{F_{\tau,q}^s(\mathbb{R}^d)} \leq C \|Ef\|_{H^{s+\varepsilon}(\mathbb{R}^d)},$$

Applying Theorem 9 of Hangelbroek and Ron [2010] with $p = 2$ to Ef , there exists a K -term Gaussian network g_K with adaptive centers and adaptive tension parameters such that

$$\|Ef - g_K\|_{L^2(\mathbb{R}^d)} \leq CK^{-s/d} |Ef|_{F_{\tau,q}^s(\mathbb{R}^d)}.$$

Combining the previous estimates gives

$$\|Ef - g_K\|_{L^2(\mathbb{R}^d)} \leq CK^{-s/d} \|f\|_{H^{s+\varepsilon}(\Omega)}.$$

Restricting the estimate to Ω yields

$$\|f - g_K\|_{L^2(\Omega)} \leq \|Ef - g_K\|_{L^2(\mathbb{R}^d)} \leq CK^{-s/d} \|f\|_{H^{s+\varepsilon}(\Omega)}.$$

Finally, isotropic Gaussians are a special case of the Gaussian primitive in (2) by choosing $\Sigma_k = \sigma_k^2 I$. Hence the same approximant belongs to \mathcal{G}_K . □

B.3 Proof of Proposition 2

We first prove a localization estimate for the normalized Gaussian Shepard weights. It states that, although each Gaussian has global support, the normalized weights concentrate their moments at scale h_K .

Lemma 8 (Moment localization). *Let $\Omega \subset \mathbb{R}^d$ be a bounded Lipschitz domain, and let $X_K = \{\boldsymbol{\mu}_k\}_{k=1}^K \subset \Omega$ be quasi-uniform. Assume further that the Gaussian amplitudes and covariances satisfy $0 < w_- \leq w_k \leq w_+ < \infty$, and $c_\Sigma h_K^2 I \preceq \Sigma_k \preceq C_\Sigma h_K^2 I, k = 1, \dots, K$ with constants c_Σ, C_Σ independent of K . Then, for every $m \geq 0$,*

$$\sup_{\mathbf{x} \in \Omega} \sum_{k=1}^K \psi_k(\mathbf{x}) |\mathbf{x} - \boldsymbol{\mu}_k|^m \leq C_m h_K^m,$$

where C_m is independent of K .

Proof. Fix $\mathbf{x} \in \Omega$. By the definition of h_K , there exists $k_{\mathbf{x}}$ such that $|\mathbf{x} - \boldsymbol{\mu}_{k_{\mathbf{x}}}| \leq h_K$.

Since $\Sigma_k \preceq C_\Sigma h_K^2 I$, $\varphi_k(\mathbf{x}) \leq \exp\left(-\frac{|\mathbf{x} - \boldsymbol{\mu}_k|^2}{2C_\Sigma h_K^2}\right)$, as a result

$$\sum_{k=1}^K w_k \varphi_k(\mathbf{x}) |\mathbf{x} - \boldsymbol{\mu}_k|^m \leq w_+ \sum_{k=1}^K \exp\left(-\frac{|\mathbf{x} - \boldsymbol{\mu}_k|^2}{2C_\Sigma h_K^2}\right) |\mathbf{x} - \boldsymbol{\mu}_k|^m.$$

Decompose the centers into annuli

$$A_n(\mathbf{x}) := \{\boldsymbol{\mu}_k : nh_K \leq |\mathbf{x} - \boldsymbol{\mu}_k| < (n+1)h_K\}, \quad n = 0, 1, 2, \dots$$

By quasi-uniformity, $q_K \gtrsim h_K$, and the number of centers in each annulus satisfies

$$\#A_n(\mathbf{x}) \leq C(n+1)^d.$$

Therefore,

$$\sum_{k=1}^K w_k \varphi_k(\mathbf{x}) |\mathbf{x} - \boldsymbol{\mu}_k|^m \leq Ch_K^m \sum_{n=0}^{\infty} (n+1)^{m+d} \exp(-cn^2).$$

Since the Gaussian $\exp(-cn^2)$ dominates any polynomial growth, the series is finite. Then

$$\sum_{k=1}^K w_k \varphi_k(\mathbf{x}) |\mathbf{x} - \boldsymbol{\mu}_k|^m \leq C_m h_K^m.$$

On the other hand, the lower covariance bound gives $\Sigma_{k_{\mathbf{x}}} \succeq c_{\Sigma} h_K^2 I$, we have $\varphi_{k_{\mathbf{x}}}(\mathbf{x}) \geq \exp(-1/2c_{\Sigma})$. Therefore, $\sum_{j=1}^K w_j \varphi_j(\mathbf{x}) \geq w_- \exp(-\frac{1}{2c_{\Sigma}})$. Dividing by the uniform lower bound on the denominator gives

$$\sum_{k=1}^K \psi_k(\mathbf{x}) |\mathbf{x} - \boldsymbol{\mu}_k|^m \leq C_m h_K^m.$$

□

We now apply the moment estimate to the scaffold $f_{\text{prim}}(x) = \sum_k \psi_k(x) f(\boldsymbol{\mu}_k)$ and prove Proposition 2.

Proof. Since $s > 1 + d/2$, Sobolev embedding gives

$$\|\nabla f\|_{L^\infty(\Omega)} \leq C \|f\|_{H^s(\Omega)}.$$

In particular, the point values $f(\boldsymbol{\mu}_k)$ are well-defined. Using the partition-of-unity property $\sum_{k=1}^K \psi_k(\mathbf{x}) = 1$, we have

$$f(\mathbf{x}) - f_{\text{prim}}(\mathbf{x}) = \sum_{k=1}^K \psi_k(\mathbf{x}) (f(\mathbf{x}) - f(\boldsymbol{\mu}_k)).$$

By the Lipschitz bound,

$$|f(\mathbf{x}) - f(\boldsymbol{\mu}_k)| \leq \|\nabla f\|_{L^\infty(\Omega)} |\mathbf{x} - \boldsymbol{\mu}_k|.$$

Therefore,

$$|f(\mathbf{x}) - f_{\text{prim}}(\mathbf{x})| \leq \|\nabla f\|_{L^\infty(\Omega)} \sum_{k=1}^K \psi_k(\mathbf{x}) |\mathbf{x} - \boldsymbol{\mu}_k|.$$

Applying Lemma 8 with $m = 1$ gives

$$|f(\mathbf{x}) - f_{\text{prim}}(\mathbf{x})| \leq C h_K \|\nabla f\|_{L^\infty(\Omega)}.$$

Taking the $L^2(\Omega)$ norm yields

$$\|f - f_{\text{prim}}\|_{L^2(\Omega)} \leq C h_K \|f\|_{H^s(\Omega)}.$$

Finally, quasi-uniformity on a fixed bounded domain gives $h_K \asymp K^{-1/d}$. Hence

$$\|f - f_{\text{prim}}\|_{L^2(\Omega)} \leq C K^{-1/d} \|f\|_{H^s(\Omega)}.$$

□

B.4 Residual Decoder

Proposition 9 (Residual expressivity). *Let \mathcal{H} be a residual decoder class dense in $L^2(\Omega; \mathbb{R}^C)$. Then, for any fixed $K \geq 1$, the sum class $\mathcal{F}_K + \mathcal{H} := \{\mathbf{u} + \mathbf{h} : \mathbf{u} \in \mathcal{F}_K, \mathbf{h} \in \mathcal{H}\}$ is dense in $L^2(\Omega; \mathbb{R}^C)$. Moreover, for any $\mathbf{f} \in L^2(\Omega; \mathbb{R}^C)$,*

$$\inf_{\mathbf{g} \in \mathcal{F}_K + \mathcal{H}} \|\mathbf{g} - \mathbf{f}\|_{L^2} \leq \min \left\{ \inf_{\mathbf{u} \in \mathcal{F}_K} \|\mathbf{u} - \mathbf{f}\|_{L^2}, \inf_{\mathbf{h} \in \mathcal{H}} \|\mathbf{h} - \mathbf{f}\|_{L^2} \right\}.$$

Proof. Since zero amplitudes are allowed, $\mathbf{0} \in \mathcal{F}_K$. Since the residual decoder can represent the zero function, $\mathbf{0} \in \mathcal{H}$. Hence

$$\mathcal{H} \subset \mathcal{F}_K + \mathcal{H}, \quad \mathcal{F}_K \subset \mathcal{F}_K + \mathcal{H}.$$

Because \mathcal{H} is dense in $L^2(\Omega; \mathbb{R}^C)$, the sum class $\mathcal{F}_K + \mathcal{H}$ is also dense. The stated inequality follows directly from the same two inclusions. □

This proposition is not a rate statement. It only records that adding the residual decoder cannot reduce the approximation class. The purpose of the Gaussian scaffold is therefore not universal approximation by itself, but to provide a compact and spatially explicit low-dimensional structure, while the residual decoder represents the remaining correction.

C Estimation Theory

We treat the bias–variance analysis per scalar component; summing over C channels introduces only a constant factor.

C.1 Bias–variance decomposition

Proof of Theorem 4

Proof. Let $f_K^* \in V_K$ be the L^2 -projection of f . Since $(f - f_K^*) \perp_{L^2} V_K$ and $(f_K^* - \hat{f}_K) \in V_K$, the Pythagorean theorem gives

$$\|f - \hat{f}_K\|_{L^2}^2 = \|f - f_K^*\|_{L^2}^2 + \|f_K^* - \hat{f}_K\|_{L^2}^2. \quad (9)$$

Bias. Since f_K^* is the L^2 -best approximation in V_K , it is bounded by the constructive approximant according to assumption (i) $f_K^* = \arg \inf_{g \in V_K} \|f - g\|_{L^2}$. This gives the bias bound $\|f - f_K^*\|_{L^2}^2 \lesssim K^{-2s/d} \|f\|_{H^{s+\varepsilon}}^2$.

Variance. Let $r_X := (r_1, \dots, r_N)^\top$ with $r_i = f(x_i) - f_K^*(x_i)$. At the observation points, $y = Ac^* + r_X + \varepsilon$. Write $P = (A^\top A)^{-1} A^\top$. Then least square coefficient is

$$\hat{c} = Py = P(Ac^* + r_X + \varepsilon) = c^* + P(r_X + \varepsilon),$$

so the coefficient error is

$$e := \hat{c} - c^* = P(r_X + \varepsilon).$$

The corresponding function error inside V_K satisfies

$$\|f_K^* - \hat{f}_K\|_{L^2}^2 = \left\| \sum_k e_k \varphi_k(x) \right\|_{L^2}^2 = \sum_{j,l} e_j e_l \int_{\Omega} \varphi_j(x) \varphi_l(x) dx = e^\top G e. \quad (10)$$

Taking expectation over the noise, and using $\mathbb{E}[\varepsilon] = 0$, we get

$$\mathbb{E}[e^\top G e] = \mathbb{E}[(r_X + \varepsilon)^\top P^\top G P (r_X + \varepsilon)] = r_X^\top P^\top G P r_X + \mathbb{E}[\varepsilon^\top P^\top G P \varepsilon]. \quad (11)$$

For the first term, residual term, by the lower spectral stability in assumption (ii) $G \succeq \frac{|\Omega|}{c_s N} A^\top A$. Therefore

$$(Pr_X)^\top G (Pr_X) \leq \frac{|\Omega|}{c_s N} (Pr_X)^\top A^\top A (Pr_X) = \frac{|\Omega|}{c_s N} \|APr_X\|_2^2 \leq \frac{|\Omega|}{c_s N} \|r_X\|_2^2,$$

where the last inequality uses that AP is the Euclidean orthogonal projection onto $\text{col}(A)$.

By assumption (iii) $\|r_X\|_2 / \sqrt{N} \lesssim \|r\|_{H^{s+\varepsilon}}$, we obtain

$$r_X^\top P^\top G P r_X \leq \frac{C_r}{c_s} \|r\|_{L^2}^2. \quad (12)$$

Thus, the residual term is controlled by the same approximation bias by definition.

For the second term, noise term, use

$$\mathbb{E}[\varepsilon^\top P^\top G P \varepsilon] = \text{tr}(P^\top G P \text{Cov}(\varepsilon)).$$

Since $\text{Cov}(\varepsilon) \preceq \sigma_{\text{noise}}^2 I_N$,

$$\mathbb{E}[\varepsilon^\top P^\top GP \varepsilon] \leq \sigma_{\text{noise}}^2 \text{tr}(P^\top GP) = \sigma_{\text{noise}}^2 \text{tr}(GPP^\top) = \sigma_{\text{noise}}^2 \text{tr}(G(A^\top A)^{-1})$$

The last equality holds for $P = (A^\top A)^{-1} A^\top$. Again by assumption (ii) $A^\top A \succeq c_s \frac{N}{|\Omega|} G$, we obtain

$$G^{1/2}(A^\top A)^{-1}G^{1/2} \preceq \frac{|\Omega|}{c_s N} I_K.$$

Thus

$$\text{tr}(G(A^\top A)^{-1}) = \text{tr}(G^{1/2}(A^\top A)^{-1}G^{1/2}) \leq \frac{|\Omega|}{c_s N} K.$$

As a results,

$$\mathbb{E}[\varepsilon^\top P^\top GP \varepsilon] \leq \frac{|\Omega|}{c_s} \sigma_{\text{noise}}^2 \frac{K}{N}. \quad (13)$$

Combining eqs. (9) to (13),

$$\mathbb{E}\|f - \hat{f}_K\|_{L^2}^2 \leq \left(1 + \frac{C_r}{c_s}\right) \|f - f_K^*\|_{L^2}^2 + \frac{|\Omega|}{c_s} \sigma_{\text{noise}}^2 \frac{K}{N}.$$

This proves the theorem. \square

C.2 Simplified Bound and Optimal K

Proof of Corollary 5.

Proof. Treating K as continuous (integer constraint contributes only a constant factor), the objective $F(K) = C_{\text{bias}}^2 K^{-2s/d} \|\mathbf{f}\|_{H^{s+\varepsilon}}^2 + C_{\text{var}} \sigma_{\text{noise}}^2 K/N$ has a unique minimiser. Setting $F'(K) = 0$ and solving gives $K^{(2s+d)/d} \propto (N/\sigma^2) \|\mathbf{f}\|_{H^{s+\varepsilon}}^2$; substituting back gives bias² \sim variance $\sim (\sigma^2/N)^{2s/(2s+d)} \|\mathbf{f}\|_{H^{s+\varepsilon}}^{2d/(2s+d)}$. \square

D Dimension-Specific Analysis

All theoretical results are parametric in d ; the two cases of practical interest specialise as follows.

Quantity	$d = 2$	$d = 3$
Fill distance	$h \sim K^{-1/2}$	$h \sim K^{-1/3}$
Unnorm. rate	$K^{-s/2}$	$K^{-s/3}$
Norm. rate	$K^{-1/2}$	$K^{-1/3}$
Optimal K^*	$(N/\sigma^2)^{1/(s+1)}$	$(N/\sigma^2)^{3/(2s+3)}$
Optimized risk scale	$(\sigma^2/N)^{s/(s+1)}$	$(\sigma^2/N)^{2s/(2s+3)}$

Concrete values for $d = 2$ (constants set to 1). For $N = 4/8/16/32$, $s = 1$: $K^* \approx 2/3/4/6$; $s = 2$: $K^* \approx 2/2/3/3$; $s = 3$: $K^* \approx 1/2/2/2$.

Concrete values for $d = 3$ (constants set to 1). For $N = 4/8/32/128$, $s = 1$: $K^* \approx 2/3/8/18$; $s = 2$: $K^* \approx 2/2/4/8$; $s = 3$: $K^* \approx 2/2/3/5$.

These values are not direct hyperparameter choices; they indicate the effective capacity scale implied by the bias–variance trade-off. In the small- N regime, only a few primitive degrees of freedom can be reliably supported by the observations. This variance bottleneck motivates using the primitives as a compact spatial scaffold, with the residual decoder carrying the remaining fine-scale correction.

E Connection to Navier–Stokes Regularity

Corollary 10 (Flow field approximation). *Consider the steady incompressible Navier–Stokes equations with small Reynolds number on $\Omega \subset \mathbb{R}^d$ ($d = 2$ or 3) with C^m boundary ($m \geq 2$). Assume a classical solution $\mathbf{u} \in H^{m+\varepsilon}(\Omega; \mathbb{R}^d)$, $p \in H^{m-1+\varepsilon}(\Omega)$. Then $\|\mathbf{u} - \mathbf{u}_K\|_{L^2} = O(K^{-m/d})$ and $\|p - p_K\|_{L^2} = O(K^{-(m-1)/d})$ (for $m \geq 3$), with estimation-optimal counts $K_{\mathbf{u}}^* \sim (N/\sigma^2)^{d/(2m+d)}$ and $K_p^* \sim (N/\sigma^2)^{d/(2(m-1)+d)}$.*

Apply Theorem 1 with $s = m$ (velocity) and $s = m - 1$ (pressure); substitute into Theorem 5. For smooth domains, smooth data, and regimes where classical steady solutions exist, such Sobolev regularity assumptions are standard in the Navier–Stokes regularity theory; see Temam Temam [2024] and Girault–Raviart Girault and Raviart [1986].

Corner singularities. At a geometric corner with interior angle θ , regularity is limited to $s < 1 + \pi/\theta$ (Grisvard Grisvard [2011]; Kozlov–Maz’ya–Rossmann Kozlov et al. [2000]): $s < 1.5$ at a sharp trailing edge ($\theta \approx 2\pi$), $s < 2$ at a blunt one ($\theta \approx \pi$). This caps the achievable rate on airfoils.

Boundary layers. Gradients scale as $\|\nabla \mathbf{u}\| \sim Re^{1/2}$ in layers of thickness $\delta \sim Re^{-1/2}$. Adaptive learned centers can concentrate near walls, paralleling mesh refinement; covering the layer volume $\sim \delta \cdot L^{d-1}$ with diameter- δ Gaussians suggests $O(Re^{(d-1)/2})$ primitives for the layer alone, though the exact scaling is geometry-dependent.

F Experimental Setup

F.1 AirfRANS

We use the AirfRANS dataset Bonnet et al. [2022] of 2D RANS simulations of NACA-series airfoils over ranges of angle of attack and Reynolds number. Each sample provides velocity (u, v) and pressure p on an unstructured mesh plus geometric fields (signed distance to surface, normal vectors). The target field is \mathbb{R}^C with $C = 3$.

Surface-pressure sensor layout. The main table uses $N = 8$ sensors at normalized arclength positions $\{0.0625, 0.1875, 0.3125, 0.4375, 0.5625, 0.6875, 0.8125, 0.9375\}$ — uniform spacing along the airfoil surface. The sensor-count ablation uses analogous schedules at $N \in \{4, 12, 16\}$.

Splits. (i) *Full-8*: all AoA and Reynolds values combined with a fixed random split. (ii) *AoA-8*: fixed Reynolds, disjoint AoA between train and test (generalization in angle of attack). (iii) *Reynolds-8*: fixed AoA, disjoint Reynolds between train and test. Split indices are frozen via JSON manifests to ensure reproducibility.

Query and evaluation. During training we sample 2,048 query points per case with 60% concentration near the airfoil surface; the surface is evaluated separately with 256 additional query points. The primary metric is relative L^2 error (“clean_recon_full”) averaged over the test set; secondary metrics are surface pressure error, drag/lift coefficients, and sensor-consistency error.

F.2 Senseiver Cylinder (Cy_Taira)

We use the Cy_Taira cylinder dataset as distributed with the Senseiver public repository Santos et al. [2023]. The field is 2D vorticity behind a cylinder at $Re = 100$. Following the Senseiver 1%-data protocol, all methods use the same fixed 50 training frames (split seed 123). The reported test metric is computed on the 4,950 non-training frames. For methods that require checkpoint selection, we use a fixed 200-frame validation subset drawn from the non-training frames; the final reported metric still follows the Senseiver 4,950-frame convention.

Interior-8 protocol. Sensor positions match the official Senseiver setting (8 interior sensors placed in the wake). For this protocol, we cite the published Senseiver number (0.039) as the comparison, and report our FLUIDSPLAT result under the same sensor layout, data protocol, and relative- L^2 evaluation metric.

Surface-4/8/16 protocol. We introduce a physically motivated protocol where sensors are placed on the cylinder wall, mirroring the AirfRANS surface-sensor scenario. The cylinder center (row 55.5, col 13.5) and radius (6 px) are determined from the NMI grid geometry (112×192); sensors are placed at evenly spaced angles and snapped to valid integer grid locations. The layouts are frozen across methods:

Layout	Grid coordinates [row, col]
Surface-4	[55,20], [49,14], [55,7], [62,13]
Surface-8	[55,20], [51,18], [49,14], [51,9], [55,7], [60,9], [62,13], [60,18]
Surface-16	[55,20], [53,19], [51,18], [50,16], [49,14], [50,11], [51,9], [53,8], [55,7], [58,8], [60,9], [61,11], [62,13], [61,16], [60,18], [58,19]

For this protocol, we run the official Senseiver code with only the sensor coordinates changed. Because the original paper does not publish a surface-sensor setting, we select a strong official-code configuration and reuse it across seeds with the same fixed 50 training frames; only the model seed is changed. Surface-4 Senseiver is evaluated at the fixed 2,200-epoch point selected by an explicit convergence sweep, while Surface-8/16 use the long official-code schedule; this prevents premature early stopping from dominating the surface comparison.

F.3 FLUIDSPLAT Implementation Details

Shared core. All experiments use the same architecture: per-sensor MLP encoder with mean/max pooling, a linear primitive head, query-to-primitive cross-attention with residual connection and feed-forward layer, and a Fourier-feature residual MLP. The decoder receives the scaffold evaluation $\mathbf{f}_{\text{prim}}(\mathbf{x})$, basis mass, global context, and cross-attention output in all cases.

Cylinder Surface-4/8/16. The primitive head predicts an anisotropic, rotated Gaussian state with $K = 256/384/448$ primitives for Surface-4/8/16 respectively. The residual path is a Fourier-feature MLP with 4 hidden layers (width 320/448/512 for Surface-4/8/16) and 6 frequency bands. A learned global token is appended. No per-query geometry features or metadata conditioning are used.

Primitive parameterization (cylinder). Centers $\mu_k \in [0, 1]^d$ (domain normalized). Scales σ_k are bounded for numerical stability: Surface-4/8 use $[0.01, 0.35]$, while Surface-16 uses the sharper range $[0.005, 0.25]$. Weights $w_k \in (0, 1)$ via sigmoid. Amplitudes $\alpha_k \in \mathbb{R}^C$ unconstrained. Rotation angle θ_k is enabled.

AirfRANS (all splits). FLUIDSPLAT uses the same scaffold-conditioned decoder as in the cylinder experiments but with axis-aligned Gaussians (rotation disabled) and lightweight domain conditioning. The decoder additionally receives 6-D per-query features (signed distance to the airfoil, nearest-surface normal, normalized arclength, and flow-frame coordinates) and featurewise metadata modulation from normalized case descriptors (Reynolds number, angle of attack; modulation gain 0.35). The Full and AoA splits use a learned global token; the Reynolds split disables it. Primitives: $K = 96$; residual MLP: 3 hidden layers, width 192/128/192 for Full/AoA/Reynolds respectively; 6 frequency bands; scale range $[0.01, 0.35]$.

Training (cylinder). Surface-cylinder runs use Adam with weight decay 10^{-6} , batch size 16, ReduceLROnPlateau (factor 0.5, patience 25), and gradient clipping. Learning rates are 8×10^{-4} for Surface-4 and 5×10^{-4} for Surface-8/16. Observation-consistency weights are $\lambda_{\text{obs}} = 0.02/0.01/0.005$ for Surface-4/8/16, respectively. Minimum training lengths are 350–500 epochs with early-stopping patience 100–180. Exact per-run configurations are archived with the experiment outputs.

Training (AirfRANS). Adam with learning rate 10^{-3} , weight decay 10^{-6} , batch size 2, ReduceLROnPlateau, gradient clipping at 1.0. $\lambda_{\text{obs}} = 0.05$ and $\lambda_{\text{surface}} = 0.2$. Early stopping patience 3 (in units of full dataset passes). Five training seeds per split for the main table; three seeds for the controlled ablation.

Compute. All experiments were run on a single NVIDIA RTX 5060 Ti (16 GB). Typical wall-clock training times per run: cylinder Surface ≈ 20 –65 min; AirfRANS ≈ 50 min per split-seed.

G Baseline Implementations

Senseiver (official / official-adapter). We run the official Senseiver public code from commit e443eb0 with only sensor coordinates changed for the surface-cylinder setting. In AirFRANS we adapt the official conditioning scheme to the AirFRANS geometry tokens; we label this variant *Senseiver official-adapter* when it is not a direct reproduction of a published experiment.

DeepONet. A branch-and-trunk architecture where the branch encodes sensor readings (coordinates + values + optional geometry tokens) and the trunk encodes normalized query coordinates with Fourier features. Not an official DeepONet release; we implement the version best suited to AirFRANS-style sparse sensing.

RecFNO (reimpl.) and FLRONet (reimpl.). Operator-style baselines. RecFNO: pooled sensor tokens \rightarrow dense latent grid \rightarrow spectral convolution \rightarrow bilinear query sampling. FLRONet: radial/softmax sensor-to-grid embedding \rightarrow CNN decoder \rightarrow bilinear sampling. We clearly label these as reimplementations; neither matches the exact architecture of any single published paper.

POD-Ridge. Classical baseline: interpolate training fields to a regular grid, take SVD to obtain POD modes, fit ridge regression from sensor values to POD coefficients, project back to the query mesh. Deterministic (no seed-level variance).

H Additional Results

H.1 Cylinder surface results: exact seed values

Table 6 lists the exact seed-level means used to compute the main cylinder table. All entries use the surface-sensor layouts and the same fixed 50-frame training split. Senseiver official uses the public code with only the surface coordinates and convergence schedule specified for this surface protocol; Surface-4 is reported at a fixed 2,200 epochs following the convergence sweep, while Surface-8/16 use the long-run official-code schedule.

Table 6: Exact per-seed relative L^2 values for the surface-cylinder protocol. These are seed-level means over the 4,950 test frames.

Setting	Method	123	124	125	126	127
Surface-4	FLUIDSPLAT (ours)	0.0679	0.0640	0.0572	0.0662	0.0654
Surface-4	Senseiver official	0.0718	0.0643	0.0940	0.0817	0.0675
Surface-4	DeepONet	0.0981	0.0925	0.0916	0.0901	0.0900
Surface-4	FLRONet (reimpl.)	0.0702	0.0688	0.0789	0.0683	0.0604
Surface-4	RecFNO (reimpl.)	0.0783	0.0542	0.0975	0.0773	0.0655
Surface-8	FLUIDSPLAT (ours)	0.0479	0.0298	0.0348	0.0361	0.0304
Surface-8	Senseiver official	0.0676	0.0603	0.0495	0.0602	0.0526
Surface-8	DeepONet	0.1272	0.1419	0.1086	0.1308	0.1420
Surface-8	FLRONet (reimpl.)	0.0579	0.0592	0.0796	0.0657	0.0766
Surface-8	RecFNO (reimpl.)	0.1138	0.0935	0.0876	0.1080	0.1092
Surface-16	FLUIDSPLAT (ours)	0.0166	0.0154	0.0170	0.0156	0.0152
Surface-16	Senseiver official	0.0571	0.0722	0.0464	0.0575	0.0450
Surface-16	DeepONet	0.0959	0.0957	0.0960	0.0950	0.0905
Surface-16	FLRONet (reimpl.)	0.0425	0.0479	0.0515	0.0448	0.0432
Surface-16	RecFNO (reimpl.)	0.0658	0.0742	0.0635	0.0723	0.0768

FLUIDSPLAT has the best five-seed mean in all three surface-sensor regimes. The strongest non-ours method changes with sensor count: FLRONet is closest at Surface-4/16, while Senseiver official is closest at Surface-8 after long convergence-controlled training.

Table 7: Exact oracle Shepard smoothing diagnostics on the Senseiver cylinder data. Smoothing is applied to the vorticity frames in grid-pixel units before the fixed-center oracle interpolation; no learned model is used.

Setting	roughness	fitted exponent	$K = 16$	$K = 128$	$K = 2048$
raw	0.5241	-0.236	1.0851 ± 0.0866	0.7452 ± 0.0189	0.4144 ± 0.0022
1px	0.3471	-0.367	1.1039 ± 0.1031	0.6703 ± 0.0229	0.2498 ± 0.0014
4px	0.1691	-0.521	1.1276 ± 0.1137	0.4897 ± 0.0254	0.1093 ± 0.0010
8px	0.1212	-0.536	1.0529 ± 0.1005	0.3527 ± 0.0119	0.0812 ± 0.0010

Table 8: Exact trained Surface-8 K-sweep values. All rows use the Senseiver cylinder data, the Surface-8 sensor layout, the fixed 50-frame training split, and evaluate relative L^2 on 4,950 held-out frames. Values are mean \pm seed standard deviation over seeds $\{123, \dots, 127\}$.

K	Full FLUIDSPLAT	Primitive-only
64	0.0282 ± 0.0017	0.3471 ± 0.0149
128	0.0287 ± 0.0015	0.2933 ± 0.0252
256	0.0298 ± 0.0033	0.2501 ± 0.0125
384	0.0358 ± 0.0073	0.2356 ± 0.0199

H.2 Senseiver interior-8: official and local reruns

For transparency we include both the published Senseiver number and our local reruns of the official Senseiver code on the interior-8 protocol:

Setting	clean_recon_full
Senseiver official (published)	0.039
Senseiver official-adapter (local rerun, 5 seeds)	0.4118 ± 0.0135
FLUIDSPLAT (ours, single run)	0.0097

The local adapter run is included only as a diagnostic: for the Interior-8 leaderboard comparison we cite the published Senseiver number, which is the most faithful representation of the original method. See Section J for the surface-protocol official-code details.

H.3 Theory-validation exact numbers

This subsection reports the exact values underlying the theory-validation figure in the main paper. The oracle smoothing diagnostic uses the official Senseiver Cy_Taira data, excludes the fixed 50 training frames, samples 30 evenly spaced held-out frames, and uses nested farthest-point centers with $\alpha = 0.3$. Smoothing applies `scipy.ndimage.gaussian_filter` with $\sigma = \text{smooth_px}$ (Gaussian kernel in grid-pixel units; 0=raw, 1, 4, 8 px). Fitted exponents are log-log linear regressions over $K \in \{16, 32, 64, 128, 256, 512, 1024, 2048, 4096, 8192\}$. The roughness column reports the normalized gradient magnitude: $\text{roughness} = \|\nabla f\|_{\text{rms}} / \|f\|_{\text{rms}}$, computed over valid grid points. This controlled smoothing diagnostic is not used in any benchmark evaluation or trained model; it exists solely to separate the smooth-field approximation mechanism from the high-frequency roughness of the unsmoothed benchmark data. The trained K-sweep uses raw data under the Surface-8 protocol.

H.4 FLUIDSPLAT K-ablation

We use K -sweeps as a model-design diagnostic rather than as a headline benchmark: the final surface-cylinder main-table runs tune K jointly with decoder width, attention dimension, scale range, and observation-consistency weight and remain fixed in the main results. The K -sweep varies only K while holding all other hyperparameters at their $K = 384$ -tuned values (residual hidden dim 448, attention dim 160, 4 heads, scale range $[0.01, 0.35]$, $\lambda_{\text{obs}} = 0.01$). In particular, Surface-8 keeps the selected $K = 384$ configuration in the main cylinder table; the smaller- K points demonstrate the single-axis effect of primitive count under otherwise fixed architecture. The diagnostic sweep illustrates that primitive-only models improve with K yet remain far worse than the full model at

all tested K , while the full model degrades at larger K , consistent with the variance bottleneck mechanism.

Configuration	Qualitative trend	Use in final model
Gaussian-only (no residual)	improves with K but remains far worse	ablation only
FLUIDSPLAT (with residual)	best at small K , degrades at large K	jointly tuned with decoder

This pattern is consistent with the bias–variance trade-off prediction: increasing primitive count alone is insufficient under sparse observations, so the final model relies on the Gaussian state for structured low-dimensional geometry and the residual decoder for high-frequency correction.

I Qualitative Reconstructions

The qualitative reconstruction figures in the main paper are generated from archived trained checkpoints and held-out samples; no additional smoothing or post-processing is applied to the predictions. The AirfRANS panel uses display-normalized centered pressure only for visual contrast: subtracting the crop median and applying a robust asymmetric display scale does not change the reconstruction error, and all quantitative tables use the original multi-channel physical field. We visualize the learned scaffold on the cylinder domain shown in Figure 5, where the regular geometry makes spatial structure directly visible. On AirfRANS, the scaffold’s interpretability derives from the same explicit parameterization (inspectable centers, scales, and amplitudes); its quantitative contribution is confirmed via ablation (Table 4).

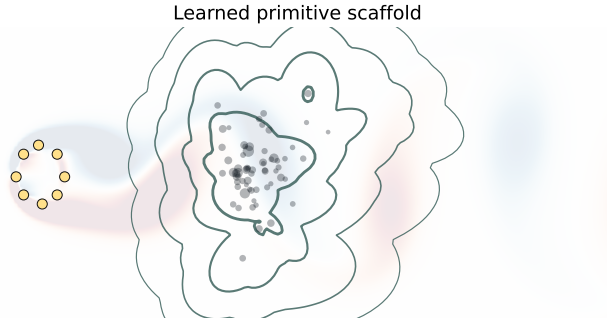


Figure 5: Appendix diagnostic for the Senseiver cylinder Surface-8 run. The panel visualizes primitive influence (maximum weighted Gaussian basis response) and the highest-weight primitive centers over a faint ground-truth vorticity context background used only for spatial reference. This is not a primitive-only prediction field; it shows how the structured latent state places support near the body and wake before the state-conditioned residual decoder forms the final reconstruction.

These qualitative panels are intentionally not presented as evidence that the Gaussian primitive field alone solves the task. Instead, they support the central interpretation used throughout the paper: primitives provide an interpretable, geometry-aware latent scaffold, whereas the state-conditioned residual decoder supplies the missing high-frequency correction. This is why the full model can track the cylinder vortex street and AirfRANS near-body pressure structure even when the primitive-only output field is too smooth.

J Senseiver Reproduction Notes

What we report vs. what Senseiver reports. The main-text Cylinder Interior-8 comparison uses the published Senseiver number (0.039) as the baseline. This avoids treating a local reproduction attempt as the official method. Importantly:

- For the Interior-8 comparison we quote the published number, avoiding any implied reproduction failure.

- For the Surface- K protocol (which has no published baseline), we run the official Senseiver code with the sensor coordinates moved to the cylinder wall, using the same fixed 50-frame training split as the other methods.

Training configuration used. For the surface protocol, seed 123 is the selected tuning-best official-code Senseiver run for each sensor count. Seeds 124–127 reuse the same selected configuration and the same fixed training frames; only the model seed changes. This gives both a best-of-five view and a seed-level stability view under the surface-sensor protocol.

Interior-8 reproduction. To verify the published Senseiver number we ran the official code on the Interior-8 layout with the default architecture (latent dim 128, 64 latents, 4 attention heads, 3 encoder layers, 2 self-attention layers per block) and the same 70/15/15 train/val/test split. Training used the Adam optimizer with an initial learning rate of 10^{-3} , ReduceOnPlateau scheduling (factor 0.5, patience 3, minimum 10^{-5}), and gradient clipping at norm 1.0. Over 5 seeds (123–127), the test-set relative L^2 error at epoch 340 is 0.0390 ± 0.0075 (mean \pm std), matching the published value.

Clarifications on naming. We use the following convention throughout the paper and appendix: “*Senseiver official*” refers to the published Senseiver Santos et al. [2023] number or to the official code with only sensor coordinates adjusted for a new protocol; “*Senseiver official-adapter*” refers to a local reproduction where architecture/hyperparameters were adapted beyond the sensor coordinates. “*RecFNO (reimpl.)*” and “*FLRNet (reimpl.)*” are our re-implementations, not official releases.